Supplementary Material for

Partitioning of tin between mafic minerals, Fe-Ti oxides and silicate melts: Implications for tin enrichment in magmatic processes

Chunxia Wei[1,2,3], Xiaolin Xiong[1,2*], Jintuan Wang[1,2*], Fangfang Huang[1,2], Mingdi Gao[1,2]

[1] State Key Laboratory of Isotope Geochemistry, Guangzhou Institute of Geochemistry, Chinese Academy of Sciences, Guangzhou 510640, China

[2] CAS center for Excellence in Deep Earth Science, Guangzhou 510640, China

[3] College of Earth and Planetary Sciences, University of the Chinese Academy of Sciences, Beijing 100049, China

Content of Supplementary Material (SM)

Fig. S9 $D_{Sn}^{Amp/melt}$ vs. pressure and melt H_2O content.

Fig. S10 D_{Sn} vs. temperature for Ti-Mag and Spl.

Fig. S11 Partial melting results.

3. Data for Tables S1–S11 (attached in the separated Excel file)

Table S1. Concentrations of major and trace elements in starting materials.

Table S2. Data for measurement of thermal gradient.

Table S3. Comparison of Sn contents measured with EPMA and those with LA-ICP-MS.

Table S4. Sn and Fe concentrations across Re and Pt capsules determined with EPMA.

Table S5. Sn and Fe concentrations in buffers oxides (ReO_2 and RuO_2) determined with EPMA.

Table S6. Major and trace element compositions of minerals analyzed with EPMA and/or LA-ICP-MS.

Table S7. Raman spectral data for Ti-magnetite and spinel.

Table S8. Major and trace element compositions of quenched glasses analyzed with EPMA and/or LA-ICP-MS.

Table S9. Melt H_2O contents measured with FTIR.

Table S10. Non-linear least squares fit to S-curve of D_{Sn} vs. fO_2 relation.

Table S11. Amphibole and biotite formula calculated from EPMA analysis data.

Table S12. $D_{Sn}^{mineral/melt}$ and $D_{Ti}^{mineral/melt}$ at Ru–RuO_2 buffered condition.

Table S13. Phase proportions and $D_{Sn}^{mineral/melt}$ values at different fO_2 during partial melting of the Rio Maria quartz diorite.

4. References Cited in This SM

1. Supplementary Text

S1. Measurement of thermal gradient in piston-cylinder experiment

Two pairs of Pt–$Pt_{90}Rh_{10}$ thermocouples were used to measure the thermal gradient of capsule (Fig. S1). The first (TC1) was positioned at the center (hotspot) of graphite furnace and the second (TC2) was located at 5 mm above the center ((Fig. S1a). The temperatures at TC1 and TC2 positions were recorded simultaneously. We used the distance of 5 mm because the longest capsules are ~10 mm in design 3 after experiments. The results show that thermal gradient was ~10 ºC /mm at 850 ºC–1000 ºC (Fig. S1b). Each capsule during experiment had symmetric temperature because the capsule was put at the center of the graphite furnace. Therefore, the thermal gradient in capsule design 3 (< 10 mm after experiment) should be < 50 ºC. For capsules in design 2 (< 8 mm after experiment) and design 1 (< 4 mm after experiment), the thermal gradient should be < 40 ºC and < 20 ºC. The real-temperature recorded by the two pairs of thermocouples from 0–1000 ºC was shown in Table S2. Considering that the metal capsules have higher thermal conductivity than the solid pressure medium, the real thermal gradients for all runs should be even smaller.

S2. Raman analyses of Fe-Ti oxides

Fe-Ti oxides in this study were identified with the WITec alpha 300R confocal Raman spectrometer, which is equipped with a 488 nm laser, a 300 mm^{-1} grating, a 100 × Zeiss objective (numerical aperture = 0.9) and a 1,600 × 200 pixels back-illuminated charge-coupled detector. To avoid drift, the spectrometer was calibrated 3

times daily using a silicon wafer. Spot Raman analyses on Fe-Ti oxides were accomplished in the wavenumber range of 50–4200 cm^{-1}, by averaging 5–10 acquisition sequences with an acquisition time of 5–10 s per sequence. The results of Raman analyses on Fe-Ti oxides are shown in Fig. S4.

S3. FTIR spectroscopy for melt H_2O contents

H_2O contents in the quenched glasses (melts) were determined with the vacuum-type Fourier-transform infrared spectrometer (FT-IR-6100 and IRT-5000), which is equipped with mid-IR light, a KBr beam splitter, and a mercury cadmium telluride (MCT) detector. Samples containing large-area clean quenched glass pools were selected to be double-polished (thickness of 100–200 μm). Then the quenched glasses were analyzed using the FTIR in transmittance mode. The spot size of the unpolarized infrared beam is 100 × 100 microns, and each infrared spectrum is obtained by 500 scans at a resolution of 4 cm^{-1}. According to the measured intensities of 5200 cm^{-1} and 4500 cm^{-1} absorption bands, the H_2O contents of quenched glasses were calculated by the Beer-Lambert law:

$$C_{H_2O^T} = 18.015 \times \frac{A_{5200}}{d \times \rho \times \varepsilon_{5230}} + 18.015 \times \frac{A_{4500}}{d \times \rho \times \varepsilon_{4500}}$$

in which $C_{H_2O^T}$ represents the total water in weight fraction; A is the peak height (cm^{-1}); d is the sample thickness (cm); ρ is the glass density (gL^{-1}); ε is the absorption coefficient ($L*mol^{-1}\ cm^{-1}$). The ρ and ε values calculations are from Ohlhorst et al. (2001) and Mandeville et al. (2002), respectively. Detailed parameters for the H_2O contents calculation can be found in Table S9.

S4. S-curve regression for $D_{Sn}^{min/melt}$ vs. fO_2 relation

We carried out regression analyses for $D_{\mathrm{Sn}}^{min/melt}$ vs. fO_2 and obtained their S-curves (Fig. 4 and 6). In magmatic systems, Sn has two oxidation states of 2+ and 4+, and the reaction describing the change of its oxidation state is:

$$Sn^{2+}O + \frac{1}{2}O_2 = Sn^{4+}O_2 \quad (1)$$

The equilibrium constant (K) for this reaction is:

$$K = (X_{Sn^{4+}O_2} \cdot \gamma_{Sn^{4+}O_2})/(X_{Sn^{2+}O} \cdot \gamma_{Sn^{2+}O} \cdot (fO_2)^{-\frac{1}{2}} \quad (2)$$

where X is the mole fraction of each Sn oxide species dissolved in the silicate melt, γ is the activity coefficient of each Sn oxide component, and fO_2 is oxygen fugacity. Assuming that γ at low Sn concentrations is constant for a given composition (Henry's Law), the equilibrium constant for reaction (1) can be simplified to:

$$K' = ([Sn^{4+}O_2]/[Sn^{2+}O]) \cdot (fO_2)^{-\frac{1}{2}} \quad (3)$$

in which $K' = K \cdot (\gamma_{Sn^{2+}O}/\gamma_{Sn^{4+}O_2})$. Note that the conversion factor from mole fractions to concentrations (in square brackets) cancels out between the numerator and denominator. The Sn concentration in a crystalline phase will be given by the sum of Sn^{2+} and Sn^{4+}, each with its own thermodynamic component:

$$Sn^{2+}_{mineral} = [Sn^{2+}O] + \sum[NO_x] \quad (4a)$$

$$Sn^{4+}_{mineral} = [Sn^{4+}O_2] + \sum[MO_x] \quad (4b)$$

where $\sum[NOx]$ and $\sum[MO_x]$ are the major-element oxide components of the "stoichiometric control" needed to form the Sn components in the crystalline phase (e.g., O 'Neill and Eggins, 2002). The bulk mineral/melt partition coefficient of Sn is defined as:

$$D_{\sum Sn}^{mineral/melt} = (Sn^{2+}_{mineral} + Sn^{4+}_{mineral})/([Sn^{2+}O]_{melt} + [Sn^{4+}O_2]_{melt}) \quad (5)$$

Substituting expression (3) into (5) to obtain the following S-type function (e.g., Mallmann and O 'Neill, 2007).

$$D_{\sum \mathrm{Sn}}^{mineral/melt} = \frac{D_{Sn^{2+}}^{mineral/melt} \cdot (K')^{-1} \cdot (fO_2)^{-\frac{1}{2}} + D_{Sn^{4+}}^{mineral/melt}}{1 + (K')^{-1} \cdot (fO_2)^{-\frac{1}{2}}} \quad (6)$$

Equation (6) can be used to fit our data and describes the sole effect of fO_2 on the Sn partitioning between crystal and silicate melt. At constant temperature and fixed melt composition, $D_{\sum Sn}^{mineral/melt}$ is controlled by three parameters: (1)$D_{Sn^{2+}}^{mineral/melt}$, the value at the reduced plateau; (2) $D_{Sn^{4+}}^{mineral/melt}$, the value at the oxidized plateau; and (3) K', the equilibrium constant of Eq. (4). We need values of the $D_{\sum Sn}^{mineral/melt}$ obtained in the experiments at least three pairs of data (D_{Sn} and fO_2) to acquire these three parameters by least square fitting (Table S10).

S5. Models for partial melting and fractional crystallization

We modelled Sn enrichments during partial melting of crustal rock and subsequent fractional crystallization of the derived magma. The Sn content in an evolved magma depends on the initial Sn content in the source rock, bulk $D_{\mathrm{Sn}}^{min/melt}$, partial melting degree, and magma fractionation degree. To simplify the model, we adopt the parameter $\frac{C_{Sn}}{C_0}$ (Sn concentration in melt /initial Sn concentration) to evaluate the Sn enrichment degrees in the two processes. The modelling methods are as follows.

(1) Selection of phase equilibria for partial melting: Geo-PS software was used to calculate mineral assemblages, mineral proportions during the protolith partial melting process.

(2) Selection of P–T paths for partial melting: The P–T path of 650–1000 °C and

1GPa was used to model melting of rocks at the lower crustal condition.

(3) Selection of mechanisms for partial melting and fractional crystallization: Batch partial melting and Rayleigh fractionation models below are adopted.

Batch partial melting equation (Shaw, 1970): $\frac{C_L^i}{C_o^i} = \frac{1}{D+F(1-D)}$

Rayleigh fractionation equation: $\frac{C_L^i}{C_o^i} = \cdot F^{D_i-1}$

where C_L^i is the weight concentration of element i in melt.

C_o^i is the weight concentration of element i in original un-melted solid (partial melting) or the weight concentration of element i in parental melt (fractional crystallization).

F is the weight fraction of melt relative to parent, representing the degree of partial melting or fractional crystallization.

D is the bulk solid-liquid partition coefficient of element i.

The average bulk partition coefficient (D) is determined using the following equation:

$$D = \sum_{x=1}^{n} Dx \cdot X$$

S6. Partition coefficients used in modelling calculations

The partition coefficients used for the modelling are selected as follows: D_{Sn} for amphibole, biotite, clinopyroxene, and orthopyroxene at different fO_2 were calculated from the S-curve equations determined by our experiments. D_{Sn} for plagioclase is a constant of 0.01 according to our experiments. Rutile and ilmenite are less important in the model for the small fraction, and their D_{Sn} was estimated by S-curve equation of Ti-magnetite for two reasons: rutile and ilmenite have similar solid-solution structure

with Ti-magnetite; $D_{Sn}^{ilmenite/melt}$ is approximate with $D_{Sn}^{Ti-magnetite/melt}$ at a certain fO_2 in our experiments. Sn in quartz should be highly incompatible and the D_{Sn} is set as 0. The D_{Sn} for garnet is from natural samples (Simons et al., 2017; Zhao et al., 2022). The bulk Sn partition coefficients are listed in Table 7 and Table S13.

2. Supplementary Figures

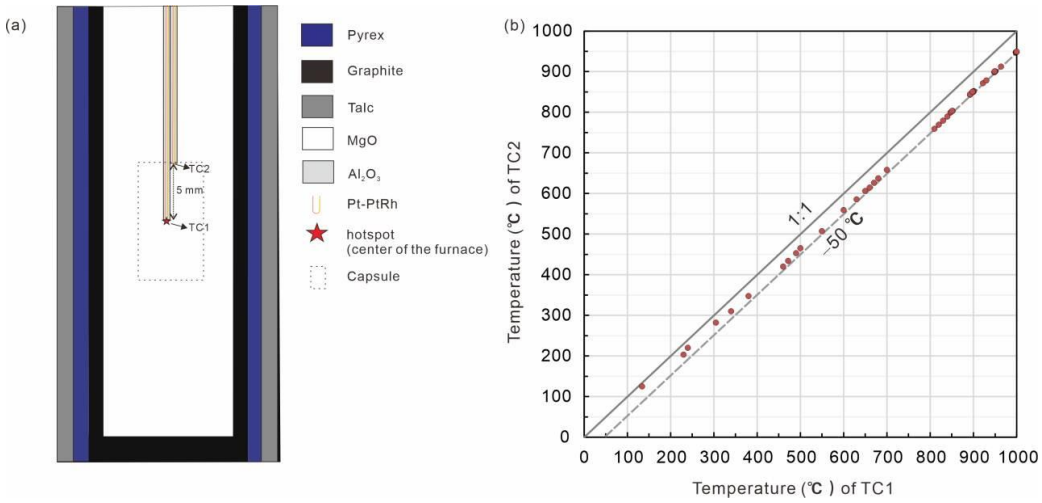

Fig. S1. Measurement of thermal gradient for the capsule design 3 in the piston-cylinder experiments. (a) Design of the experimental assembly, showing the desired thermocouple positions (TC1 and TC2). (b) Temperature measurements at the center of the furnace (TC1, hot spot) and at 5 mm above the hot spot (TC2), showing that the thermal gradient is 10 ℃/mm in the furnace. Data from Table S2 in the separated Excel file.

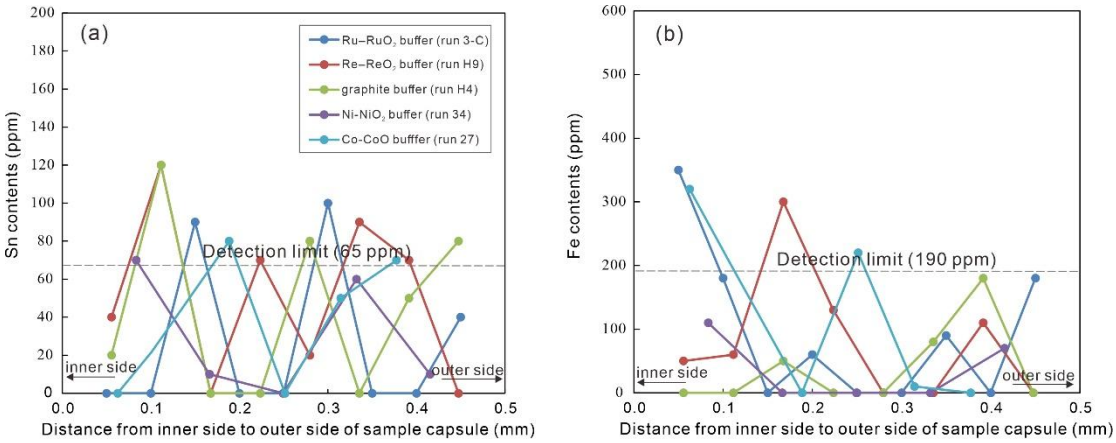

Fig. S2. Sn (a) and Fe (b) concentration profiles determined across sample capsules (Re or Pt capsule) from inner side (close to glasses) to outer side of capsules, showing limited loss of Sn and Fe to the sample capsules. The detection limit of Sn is ~65 ppm and Fe is ~190 ppm by using EPMA. Data from Table S4 in the separated Excel file.

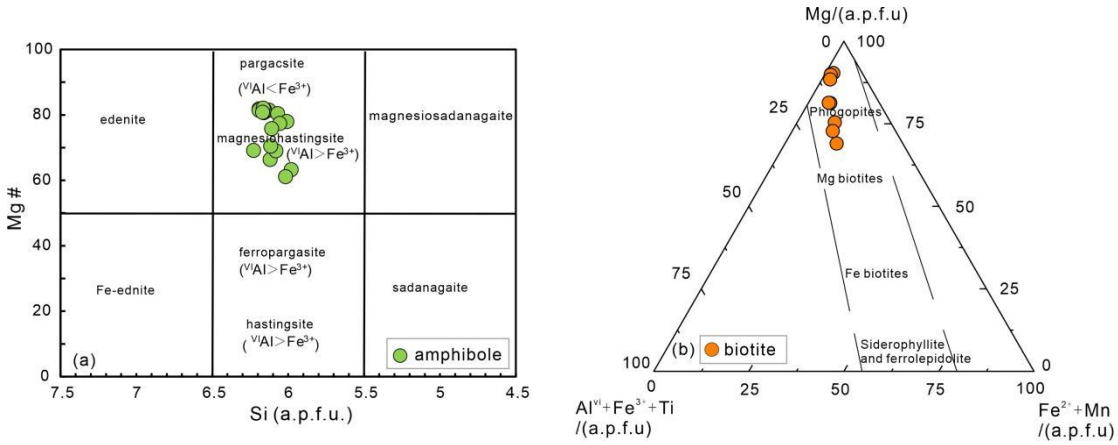

Fig. S3. Classification diagrams of amphibole (a) (Leake et al., 1997) and biotite (b) (Foster, 1960), showing that the amphiboles are pargasite and magnesio-hastingsite and the biotites are phlogopite in this study. Data from Table S11 in the separated Excel file.

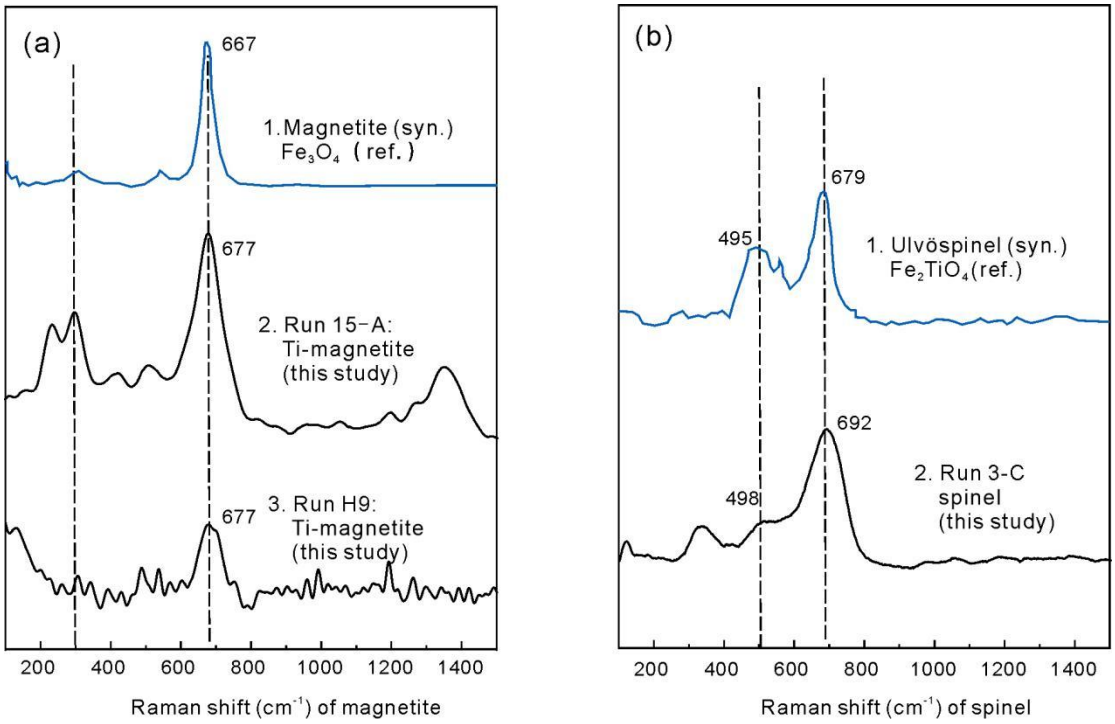

Fig. S4. Raman shifts of magnetite (a) and spinel (b) in Wang et al. (2004) (blue curves) and this study (black curves). Curve-fitting of the spectra reveals their major Raman A1g peak position of ~670 cm^{-1} for magnetite, ~690 cm^{-1} for ilmenite and ~680 cm^{-1} for spinel. Data from Table S7 in the separated Excel file.

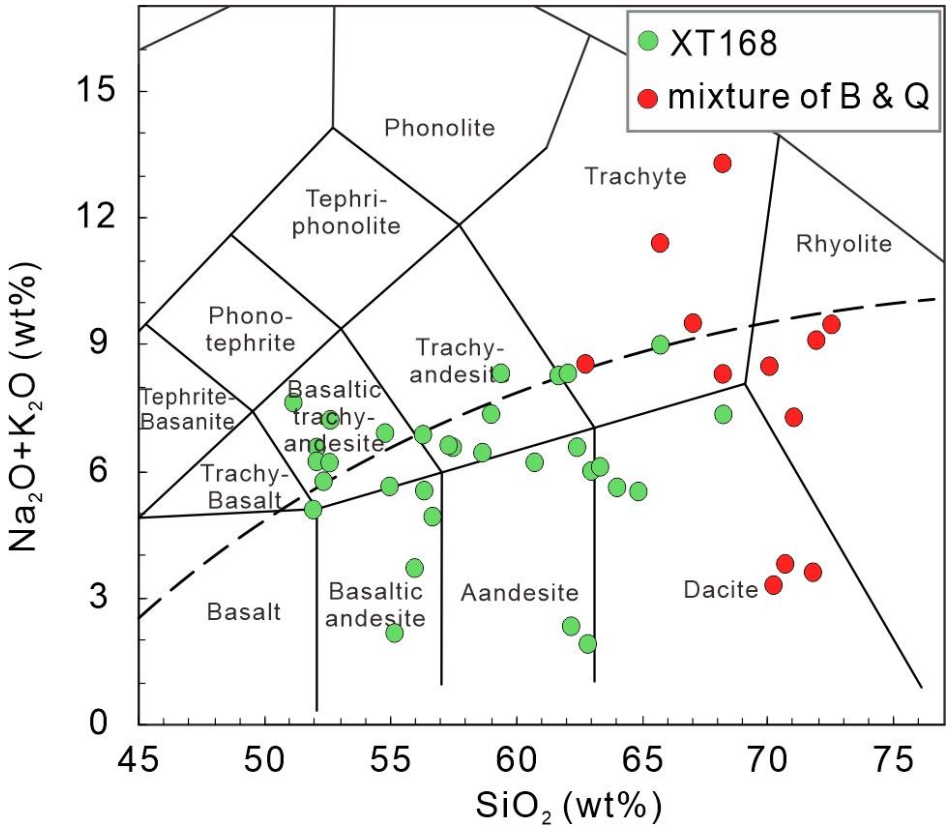

Fig. S5. Total alkali (Na_2O+K_2O) vs. SiO_2 (Le Maitre et al., 1989) of the quenched glasses on the anhydrous basis (EPMA analyses normalized to 100%), showing that the compositions of the run product glasses vary from basaltic andesite to rhyolite. The blue symbols represent set 1 experiments (XT168 as starting material) and the red symbols represent set 2 experiments (mixtures of B & Q as starting materials). Data from Table 5 in the main text.

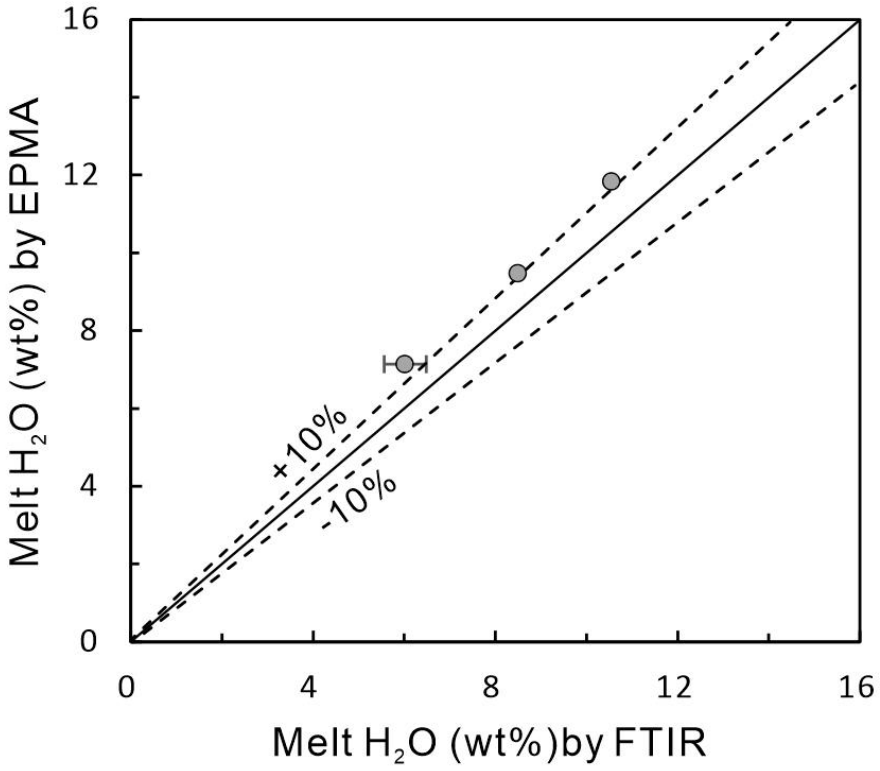

Fig. S6. Comparison of melt H_2O contents measured using FTIR and melt H_2O contents calculated from the difference of EPMA total from 100%, showing that the calculated melt H_2O contents are consistent within ~10% error with melt H_2O contents measured using FTIR. Data from Table S9 in the separated Excel file.

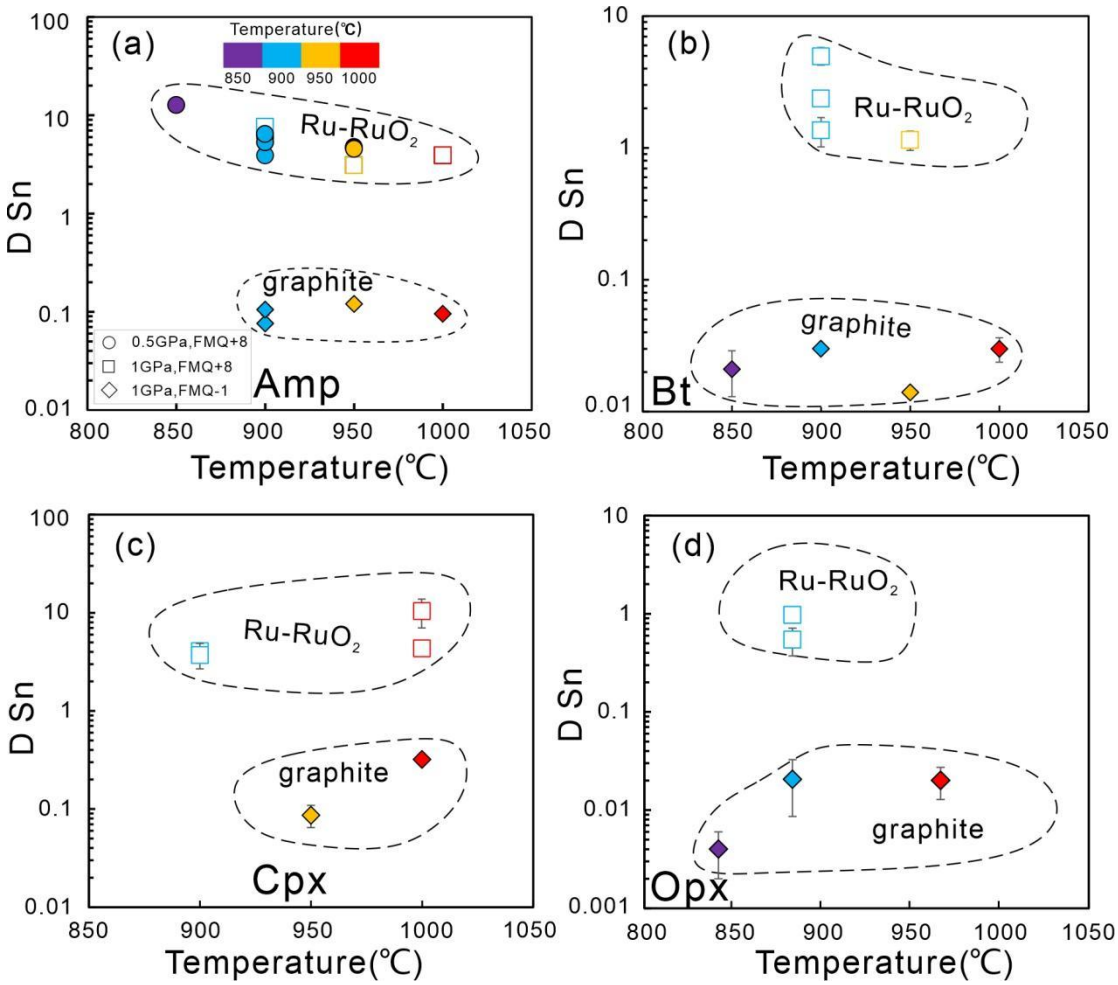

Fig. S7. D_{Sn} vs. temperature for amphibole (a), biotite (b), clinopyroxene (c) and orthopyroxene (d). The panel (a) shows that $D_{Sn}^{Amp/melt}$ decrease with increasing temperature under the Ru–RuO_2 buffered conditions. D_{Sn} data from Table 6 in the main text.

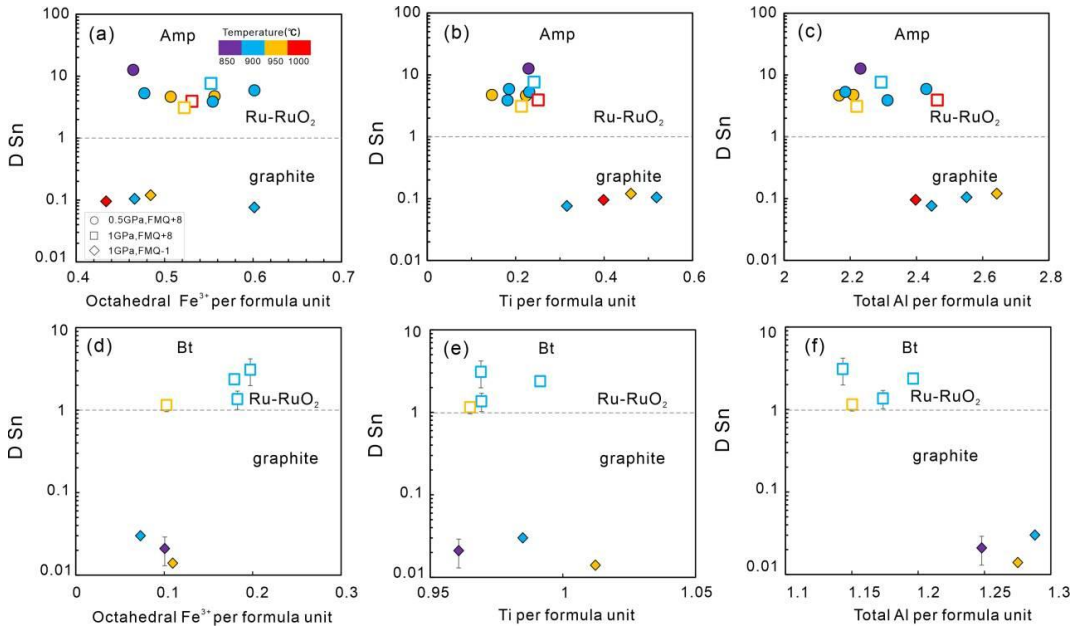

Fig. S8. D_{Sn} vs. octahedral Fe^{3+}, Ti and Al per formula unit for amphibole (a–c) and biotite (d–f) under Ru–RuO_2 and graphite buffered conditions. No correlations on these panels suggest the negligible effect of mineral composition on the Sn partitioning. Data from Table 6 in the main text and Table S11 in the separated Excel file.

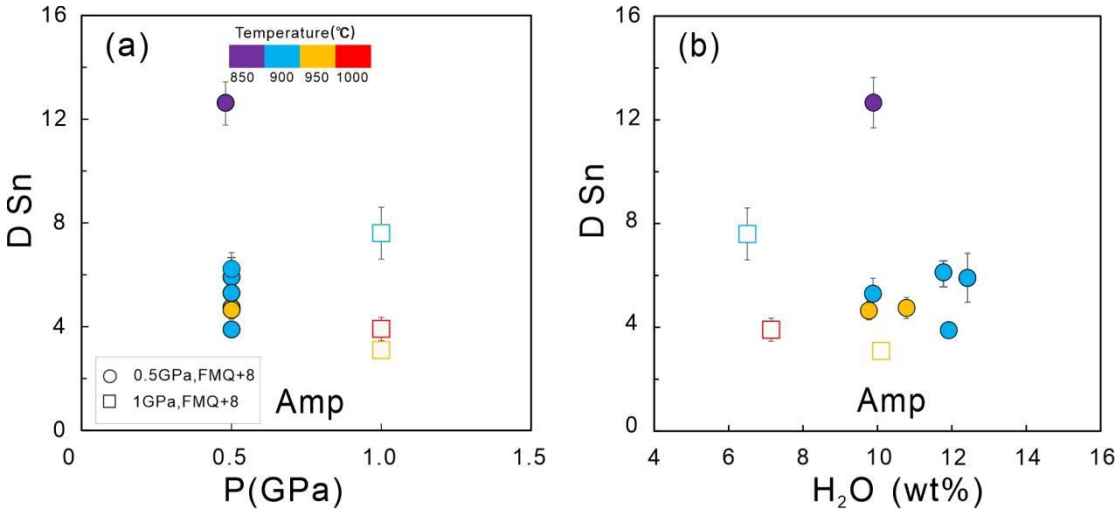

Fig. S9. $D_{Sn}^{Amp/melt}$ vs. pressure (a) and melt H_2O content (b) in the Ru–RuO_2 buffered runs, showing no correlations between $D_{Sn}^{Amp/melt}$ and pressure or melt H_2O content. Partition coefficients data from Table 6 in the main text.

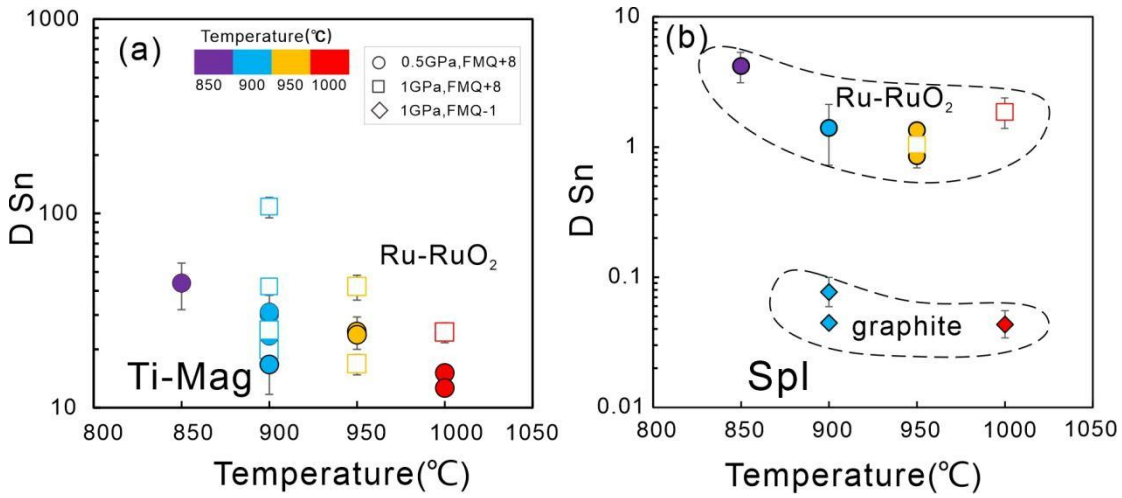

Fig. S10. D_{Sn} vs. temperature for Ti-magnetite (a) and spinel (b), showing that the D_{Sn} values decrease with increasing temperature under the Ru–RuO_2 and graphite buffered conditions. Data from Table 6 in the main text.

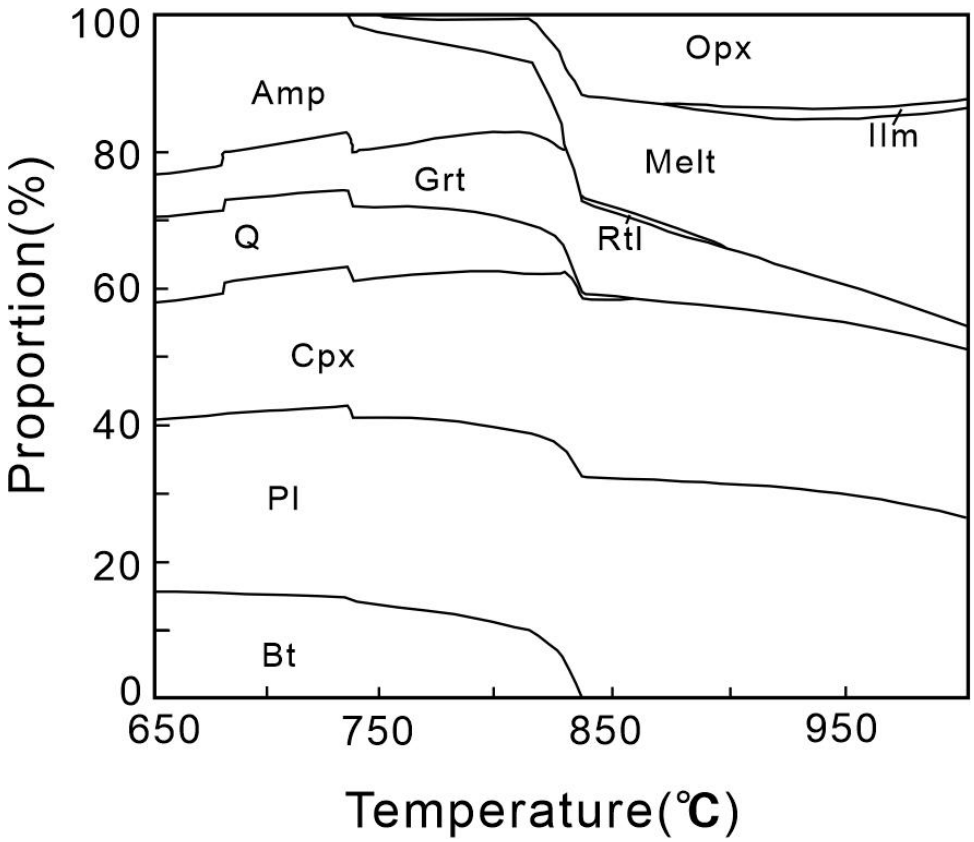

Fig. S11. Partial melting results of Rio Maria quartz diorite at 1 GPa, showing proportions of phases as the function of temperature. Mineral abbreviations as in Table 2 of the main text. Data from Table S13 in the separated Excel file.

References Cited in SM

Foster, M.D., 1960. Interpretation of the composition of trioctahedral micas. U.S. Geological Survey Professional Paper 354-B, 1–146.

Le Maitre, R.W.B., Dudek, P., Keller, A., Lameyre, J., Le Bas, J., Sabine, M.J., Schmid, P.A., Sorensen, R., Streckeisen, H., Woolley, A., 1989. A classification of igneous rocks and glossary of terms: Recommendations of the International Union of Geological Sciences, Subcommission on the Systematics of Igneous Rocks. International Union of Geological Sciences.

Leake, B.E., Woolley, A.R., Arps, C.E.S., Birch, W.D., Gilbert, M.C., Grice, J.D., Hawthorne, F.C., Kato, A., Kisch, H.J., Krivovichev, V.G., Linthout, K., Laird, J., Mandarino, J.A., Maresch, W.V., Nickel, E.H., Rock, N.M.S., Schumacher, J.C., Smith, D.C., Stephenson, N.C.N., Ungaretti, L., Whittaker, E.J.W., and Youzhi, G.,1997. Nomenclature of amphiboles: Report of the Subcommittee on Amphiboles of the International Mineralogical Association, Commission on New Minerals and Mineral Names. Am. Mineral. 82, 1019–1037.

Mandeville C. W., Webster J. D., Rutherford M. J., Taylor B. E., Timbal A., Faure K. F., 2002. Determination of molar absorptivities for infrared absorption bands of H_2O in andesitic glasses. Am. Mineral. 87, 813–821.

Mallmann, G., O'Neill, H.St.C., 2007. The effect of oxygen fugacity on the partitioning of Re between crystals and silicate melt during mantle melting. Geochim. Cosmochim. Acta. 71, 2837–2857.

Ohlhorst S., Behrens H., Holtz F., 2001. Compositional dependence of molar

absorptivities of near-infrared OH- and H_2O bands in rhyolitic to basaltic glasses. Chem. Geol. 174,520.

O'Neill, H.S.C. and Eggins, S.M., 2002. The effect of melt composition on trace element partitioning: an experimental investigation of the activity coefficients of FeO, NiO, CoO, MoO_2 and MoO_3 in silicate melts. Chem. Geol. 186, 151-181.

Shaw, D.M., 1970. Trace element fractionation during anatexis. Geochim. Cosmochim. Acta v. 34, p. 237–243.

Simons, B., Andersen, J.C.Ø., Shail, R.K., Jenner, F.E., 2017. Fractionation of Li, Be, Ga, Nb, Ta, In, Sn, Sb, W and Bi in the peraluminous Early Permian Variscan granites of the Cornubian Batholith: Precursor processes to magmatic-hydrothermal mineralisation. Lithos 278–281, 491–512.

Wang, A., Kuebler, K.E., Jolliff, B.L., & Haskin, L.A. (2004). Raman spectroscopy of Fe-Ti-Cr-oxides, case study: Martian meteorite EETA79001. Am. Mineral. 89, 665–680.

Zhao, P., Yuan, S., Williams-Jones, A.E., Romer, R.L., Yan, C., Song, S., Mao, J., 2022. Temporal Separation of W and Sn Mineralization by Temperature-Controlled Incongruent Melting of a Single Protolith: Evidence from the Wangxianling Area, Nanling Region, South China. Econ. Geol. 117, 667–682.